It is noteworthy that only the relative value of $N(z)$ is used in Eq. (10.16) and $T(z)$ is therefore independent of the normalization of the density profile at $z_{\text{ref},1}$ in a first-order approximation, i.e., when a model atmosphere is used to calculate the Rayleigh extinction of the signal in Eq. (10.3).

In principle, the reference altitude $z_{\text{ref},2}$ can be chosen at the upper or at the lower boundary of the altitude range in which the integration-technique measurements are made. The data are then derived successively downward or upward, respectively. However, $T(z_{\text{ref},2})N(z_{\text{ref},2})$ must be highly accurate if profiles are to be generated upward because errors build up exponentially. On the other hand, when an upper reference height is chosen and the data are derived downward, errors in $T(z_{\text{ref},2})N(z_{\text{ref},2})$ become quickly smaller. Due to this, $T(z_{\text{ref},2})$ and $N(z_{\text{ref},2})$ are usually taken at the upper boundary of the lidar data, e.g., from a climatological model atmosphere or from collocated measurements with other instruments like resonance fluorescence lidar or airglow imagers.

Errors which are caused by the initialization with $T(z_{\text{ref},2})N(z_{\text{ref},2})$ were investigated, e.g., by Leblanc et al. [9] for downward integration. The authors used simulated data which were 15 K above the model atmosphere for all heights and found that the 15-K initialization error at 90 km decreased to 4 K at 80 km and to 1 K at 70 km. For real measurements the reference-height value should be much closer to the correct data than in this worst-case scenario so the actual downward-integration errors should be considerably smaller. It must be noted in this context that, when altitude-dependent signal-induced noise is present in the signals, inaccurate background subtraction can cause large errors. Signal-induced noise, when present, must be identified, and the data must be corrected.

The pressure profile $p(z)$ is related to $N(z)$ and $T(z)$ via Eq. (10.5). Other formalisms which derive first a pressure profile and then the temperature profile [10] are equivalent to the algorithm discussed here.

10.3.2 Applications

Atmospheric temperature profiling with the lidar integration technique started in pre-laser times. As early as 1953, Elterman utilized a searchlight to obtain molecular density profiles. Via initialization with radiosonde data and the use of "physically acceptable" lapse rates,

he obtained temperature profiles up to 67.6 km [11, 12] and studied seasonal trends of temperature, density, and pressure [13]. First measurements with laser light were done in the 1960s with a Q-switched ruby laser by Sanford and reported in an early review paper [14]. At the beginning of the 1970s, pioneering integration-technique measurements with inelastic signals were carried out by Fiocco et al. [15]. These authors used a single-mode continuous-wave argon-ion laser to measure temperature and backscatter ratio in the troposphere. The particle backscattering contribution to the molecular signal was reduced with a Fabry–Perot interferometer. Later attempts to measure temperature profiles with Cabannes scattering and to block the particle backscatter signal with a Michelson interferometer did not succeed [16]. With the use of broadband dye lasers (which were originally developed for Na and Li density measurements in the mesosphere) Hauchecorne and Chanin obtained the first lidar temperature profiles between 35 and 70 km height [10] by detecting the Rayleigh backscatter signal from the middle atmosphere. In these altitudes there are virtually no particles present which at low heights perturb the measurements. Following this breakthrough, better-suited laser types like frequency-doubled Nd:YAG [17] and excimer lasers [18] were soon employed. In the following years, the high precision of these measurements which did not need to be calibrated and the ease of implementation of the technique on existing lidar systems started the study of a wide range of geophysical phenomena. These included gravity waves [19–22], stratospheric warming and planetary waves [23, 24], semi-diurnal and diurnal thermal tides [25–29], mesospheric inversions [30, 31], the oscillation of the 27-day solar cycle [32], the influence of the 11-year solar cycle [33, 34], climatology [35, 36], and long-term trends [37]. To ensure the quality of the measured data, sources of possible errors were investigated in detail [9, 38]. Rayleigh lidar systems serve today to evaluate and validate middle-atmosphere temperature measurements from satellites and are core instruments in the Network for the Detection of Stratospheric Change (NDSC).

10.4 Rotational Raman Lidar

10.4.1 Brief Historical Survey

The use of RR backscatter signals for atmospheric temperature profiling with lidar was originally proposed in 1972 by Cooney [39]. First

boundary-layer measurements were made with interference filters in the 1970s [40, 41] and later also with grating spectrometers [42]. With subsequent improvements in laser and receiver technology, the measurement range could be extended into the stratosphere [43, 44] and semi-automated, quite robust systems for tropospheric profiling were set up [45]. Advances in interference filter manufacturing allow today the design of receiver systems with very low losses in the separation of the lidar signals and massive reduction of the elastic backscatter crosstalk so measurements can be made even in clouds with a backscatter ratio of more than 50 without the need for corrections [46]. These systems can be built sufficiently rugged to work reliably under harsh conditions during field campaigns. The temporal resolution of today's most powerful systems is a few minutes within the troposphere at a height resolution of $\sim$100 m and a measurement uncertainty of $\sim\pm1$ K [47, 48]. The measurement range of these instruments extends up to the stratopause region for night-integrated observations. As an alternative to interference filters, double-grating spectrometers are also in use today which yield similar blocking power at slightly lower cost but also have lower receiver efficiency. A high-power interference-filter-based system can also measure in the daytime [47]. To improve the daytime performance, either a transmitter that emits at short wavelengths in the solar-blind spectral region [49] or a narrow-field-of-view receiver can be used. Furthermore, the spectural bandwidth of the receiver can be narrowed by separating the N_2 RR lines by means of a Fabry–Perot interferometer (FPI) [50]. A first attempt using UV radiation from a narrow-band Raman-shifted KrF excimer laser and a thallium atomic vapor filter to block the elastic backscatter signal yielded measurements up to 1800 m height, but with large deviations of ±10 K [51] from the data of a local radiosonde. The approach using an FPI succeeded in measurements throughout the troposphere with results very close to the data of a reference sonde [52]. The RR technique can conveniently be combined with other lidar techniques, thus allowing the setup of multiparameter Raman lidar systems. Standard laser sources with high emission power can be used with—as the only non-standard feature—frequency stabilization by injection seeding; this is very helpful for obtaining a stable calibration function. RR lidars have been used successfully for the investigation of a number of geophysical phenomena. One of the first and which is still in progress was the formation of polar stratospheric clouds in the arctic winter [53, 54]; here the unique capability of RR lidar to allow continuous monitoring of optical

particle properties and temperature in the same air masses proves highly beneficial.

10.4.2 Theory

In this section, a summary of the equations that describe the intensity of the atmospheric rotational Raman (RR) backscattering is given. The theory of Raman scattering is described in more detail in Chapter 9.

For simulation studies of RR temperature lidar, it is generally sufficient to consider air as a constant mixture of nitrogen and oxygen with relative volume abundances of 0.7808 and 0.2095, respectively. The remaining gases need not be considered. This also applies to water vapor. Its RR cross section is not much larger than the cross sections of N_2 and O_2 [55], but its relative amount is quite low even in conditions of water vapor saturation. Nitrogen and oxygen molecules can be treated here as simple linear molecules (SLM), i.e., linear molecules with no electronic momentum coupled to the scattering.

The rotational energy $E_{rot,i}(J)$ of a homonuclear diatomic molecule (like molecular nitrogen and oxygen) in the rotational quantum state J is [56]

$$E_{rot,i}(J) = [B_{0,i}J(J+1) - D_{0,i}J^2(J+1)^2]hc, \ J = 0, 1, 2, \ldots, \tag{10.17}$$

where h is Planck's constant, c is the velocity of light, and i denotes the atmospheric constituent. $B_{0,i}$ and $D_{0,i}$ are the rotational constant and centrifugal distortion constant for the ground state vibrational level. On the frequency scale, the shift of the rotational Raman lines is independent of the wavelength of the exciting light λ_0. For the Stokes branch it is given by

$$\Delta\nu_{St,i}(J) = -B_{0,i}2(2J+3) + D_{0,i}[3(2J+3) + (2J+3)^3],$$
$$J = 0, 1, 2, \ldots \tag{10.18}$$

and for the anti-Stokes branch by

$$\Delta\nu_{ASt,i}(J) = B_{0,i}2(2J-1) - D_{0,i}[3(2J-1) + (2J-1)^3] \quad \text{with}$$
$$J = 2, 3, 4, \ldots. \tag{10.19}$$

The differential backscatter cross section for single lines of the pure rotational Raman spectrum can be written as [57]

$$\left(\frac{d\sigma}{d\Omega}\right)_{\pi}^{RR,i}(J) = \frac{112\pi^4}{15}\frac{g_i(J)\,h\,c\,B_{0,i}(\nu_0 + \Delta\nu_i(J))^4\,\gamma_i^2}{(2I_i + 1)^2\,k\,T}$$
$$\times\,X(J)\exp\left(-\frac{E_{rot,i}(J)}{kT}\right) \qquad (10.20)$$

where for the Stokes branch

$$X(J) = \frac{(J+1)(J+2)}{2J+3} \quad \text{with} \quad J = 0, 1, 2, \ldots \qquad (10.21)$$

and for the anti-Stokes branch

$$X(J) = \frac{J(J-1)}{2J-1} \quad \text{with} \quad J = 2, 3, 4, \ldots. \qquad (10.22)$$

$g_i(J)$ is the statistical weight factor which depends on the nuclear spin I_i. ν_0 denotes the frequency of the incident light, γ_i is the anisotropy of the molecular polarizability tensor, k is Boltzmann's constant and T is temperature. Equation (10.20) is valid if both polarization components of the RR signals are detected with the same efficiency in the lidar receiver. The depolarization of the pure rotational Raman wings is 3/4 [55], i.e., for linearly polarized incident light, a fraction of 4/7 of the backscatter signal intensity is polarized parallel and 3/7 perpendicular to the polarization plane of the incident light. To provide high signal intensities, RR lidars are usually designed to detect both polarization components with high efficiency.

The number of photons detected in an RR channel can be calculated with

$$S_{RR}(z) = S_0\varepsilon\frac{A\,O(z)}{(z-z_0)^2}\Delta z N(z)\left[\sum_{i=O_2,N_2}\sum_{J_i}\tau_{RR}(J_i)\eta_i\left(\frac{d\sigma}{d\Omega}\right)_{\pi}^{RR,i}(J_i)\right]$$
$$\times\,\tau_{atm}(z_0,z)^2 \qquad (10.23)$$

where S_0 is the number of transmitted photons, ε is the detector efficiency, A is the free telescope area, $O(z)$ describes the overlap between transmitted laser beam and telescope, Δz is the height resolution, $N(z)$ is the spatial density of air molecules, $\tau_{RR}(J_i)$ is the transmission of the receiver at the wavelength of the RR line J_i, η_i is the relative
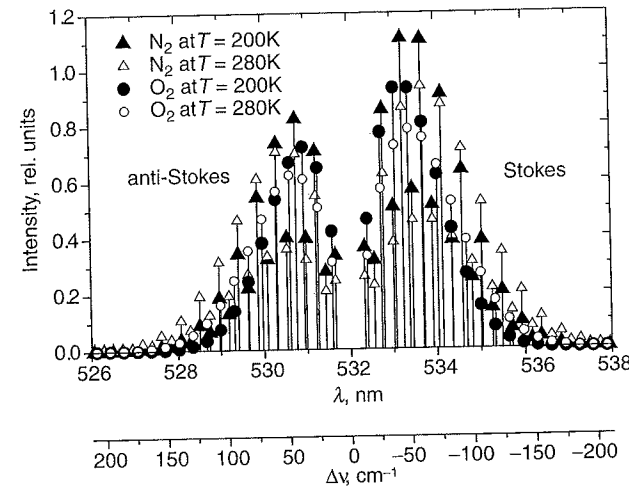
Fig. 10.1. Pure rotational Raman spectrum of air calculated for temperatures of $T = 200\,K$ and $T = 280\,K$ (intensity in relative units). The wavelength scale is for a laser wavelength of 532 nm.

volume abundance of N_2 and O_2, respectively, and $\tau_{atm}(z_0, z)^2$ is the atmospheric roundtrip transmission.

Figure 10.1 shows the pure rotational Raman spectrum of air calculated for two temperatures, 200 and 280 K. The values employed for $B_{0,i}$, $D_{0,i}$, $g_i(J)$, I_i, and γ_i^2 are listed in Table 10.2. For simplicity, the cgs units used by the authors are quoted. In Chapter 9 it is shown how these values can be transformed into the SI system. γ_i depends weekly on wavelength [$\gamma_{O_2}(\lambda = 488\,nm)/\gamma_{O_2}(\lambda = 647.1\,nm) = 1.17 \pm 11\%$; $\gamma_{N_2}(\lambda = 488\,nm)/\gamma_{N_2}(\lambda = 647.1\,nm) = 1.13 \pm 11\%$] and is considered as constant with temperature in this context [57].

Table 10.2. Ground-state rotational and centrifugal distortion constants $B_{0,i}$ and $D_{0,i}$, statistical weight factors $g_i(J)$, nuclear spin I_i, and the square of the anisotropy of the molecular polarizability tensor γ_i^2.

Molecule	$B_{0,i}$ (cm^{-1})	$D_{0,i}$ (cm^{-1})	$g_i(J)$ J even	$g_i(J)$ J odd	I_i	γ_i^2 (cm^6)
N$_2$	1.98957 [60]	5.76×10^{-6} [60]	6	3	1	0.51×10^{-48} [61]
O$_2$	1.43768 [56]	4.85×10^{-6} [56]	0	1	0	1.27×10^{-48} [61]

For RR temperature lidar the splitting of the O_2 RR lines in triplets [58] can be neglected because the two satellite lines located close to the main lines, at distances of 0.056 nm on either side, have intensities of only about 3% of the intensity of each central line. Pressure broadening of the RR lines [43] can also be disregarded when the transmission bands of the filters are broad compared to the width of the lines, which is ~ 2 GHz. (With a suitable narrow-band receiver, however, one could also make use of the pressure broadening and measure temperature and pressure simultaneously [59].)

For atmospheric temperature profiling with the rotational Raman technique, usually the ratio

$$Q(T, z) = \frac{S_{RR2}(T, z)}{S_{RR1}(T, z)} \qquad (10.24)$$

is used with S_{RR1} and S_{RR2} for two pure-rotational Raman signals of opposite temperature dependence. (One can also combine the signals in other ways which, however, gives no advantages.) In the ratio, altitude-dependent factors of the lidar equation cancel. For this it is assumed that the overlap functions are the same. For well aligned systems, this is the case above a certain minimum height. It is also assumed that atmospheric extinction of both signals is the same. Then the temperature dependence of the ratio Q is given by

$$Q(T) = \frac{\sum_{i=O_2, N_2} \sum_{J_i} \tau_{RR2}(J_i)\eta_i \left(\frac{d\sigma}{d\Omega}\right)_\pi^{RR,i}(J_i)}{\sum_{i=O_2, N_2} \sum_{J_i} \tau_{RR1}(J_i)\eta_i \left(\frac{d\sigma}{d\Omega}\right)_\pi^{RR,i}(J_i)} \qquad (10.25)$$

where the formula for the Stokes or anti-Stokes differential backscatter coefficients have to be inserted depending on which branch of the pure RR spectrum is used. $\tau_{RR1}(J_i)$ and $\tau_{RR2}(J_i)$ are the transmissions of the lidar receiver at the wavelength of the rotational Raman line J_i. Figure 10.2 shows typical temperature dependencies of the RR signals used for atmospheric temperature measurements.

In order to provide the atmospheric temperature profile, $Q(T)$ must be calibrated. The calibration can be done by characterizing the system parameters and using Eq. (10.25). This approach, however, may yield uncertainties on the order of a few K [44]. In practice, RR temperature lidar is therefore calibrated by comparison with data measured with other instruments such as local radiosondes; the temperature data of today's
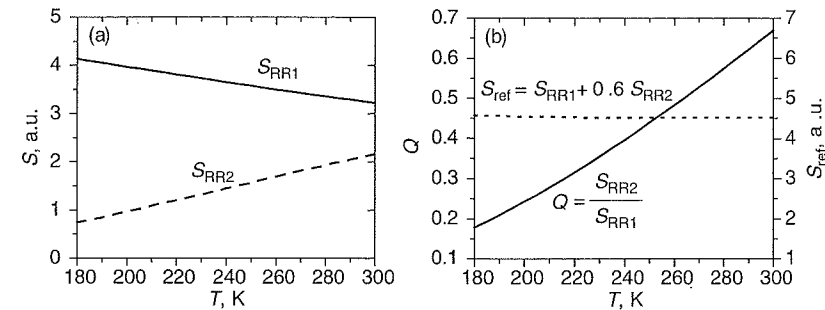
Fig. 10.2. (a) Typical intensities of the two pure-rotational Raman signals S_{RR1} and S_{RR2} as a function of temperature T [48]. (b) Signal ratio Q from which the atmospheric temperature is derived. S_{ref} can be used as a temperature-independent Raman reference signal for measuring extinction and backscatter coefficients of aerosols and cloud particles [47].

state-of-the-art radiosondes are accurate within tenths of a K provided the radiosonde itself has been accurately calibrated. Of course, the reference data used for the calibration should be taken as close in space and time as possible to the atmospheric column sensed by the lidar. How often an RR lidar systems needs to be recalibrated depends on the individual system. Provided that rugged mounts are used and the alignment of the lidar is not changed intentionally, the calibration of today's state-of-art systems remains virtually unchanged and only long-term degradations of the optical components may require recalibrations on a longer time scale.

For systems that detect only one RR line in each of the two RR channels Eq. (10.25) takes the simple form

$$Q(T) = \exp(a - b/T), \qquad (10.26)$$

where the parameters a and b are both positive if $J(S_{RR2}) > J(S_{RR1})$. b is simply the difference of the rotational Raman energies of the extracted lines divided by k, and a is the logarithm of the ratio of all factors except the exponential term in Eq. (10.20). It is straightforward to use Eq. (10.26) also for systems with several lines in each of the RR signals [42]. But the obvious inversion of Eq. (10.26) which gives

$$T = \frac{b}{a - \ln Q} \qquad (10.27)$$

then turns out to yield significant measurement errors, well in excess of 1 K (cf. Fig. 10.3) when measurements are made over an extended
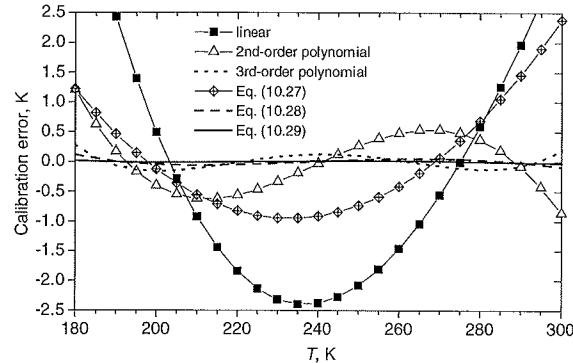
Fig. 10.3. Errors made with different calibration functions for rotational Raman temperature lidar.

range of temperatures. As the errors behave nearly as a second-order-polynomial function of temperature, it has been proposed to minimize calibration errors by a second calibration with such a second-order polynomial [43, 62], leading to a calibration function of the form

$$T = \frac{b}{a - \ln Q} + c \left(\frac{b}{a - \ln Q} \right)^2 + d \qquad (10.28)$$

with the additional calibration constants c and d.

An even better calibration function, however, is found in the approach

$$Q = \exp \left(\frac{a'}{T^2} + \frac{b'}{T} + c' \right) \Longleftrightarrow T = \frac{-2a'}{b' \pm \sqrt{b'^2 - 4a'(c' - \ln Q)}}, \qquad (10.29)$$

which extends Eq. (10.26) to a second-order term in T and needs only three calibration constants a', b', c'. Fitting, as an example, the curve $T(Q)$ shown in Fig. 10.2 with the different calibration functions, one gets the calibration errors shown in Fig. 10.3. The performances of polynomial calibration functions are also given for comparison. The single-line approach of Eq. (10.27) results here in errors of $\sim \pm 1$ K for temperatures between 180 and 285 K, which is better than a linear calibration function. However, this relation is not generally valid [63]. For three calibration constants, Eq. (10.29) is superior to the second-order polynomial and even better than the third-order polynomial and the approach of Eq. (10.28), which both require four calibration constants. For Eq. (10.29), the temperature derived from the data with that

calibration function differs from the input temperature of the simulation by less than ± 0.03 K for temperatures between 180 and 300 K. With Eq. (10.28) or the third-order polynomial approach, the deviations are about ± 0.10 K and ± 0.15 K, respectively.

In conclusion, when data that cover a large range of temperatures (>50 K) are available for the calibration, Eq. (10.29) is the best-suited calibration of RR temperature lidar when several RR lines are sampled with each channel. Otherwise the single-line approach of Eq. (10.27) should be used to avoid large extrapolation errors.

10.4.3 Technological Considerations

Laser Wavelengths

Because it combines high output power with reliability and ease of handling, the Nd:YAG laser is at present the most widely used light source for Raman lidar systems. We theoretically investigate in the following the performance of RR temperature lidar with frequency-doubled and frequency-tripled radiation of a Nd:YAG laser, i.e., 355 nm and 532 nm. The fundamental emission at 1064 nm is less suitable because of low RR backscatter cross-sections and poorer detector efficiencies at this wavelength. Measurements with the fourth harmonic at 266 nm are limited to short range because light of this wavelength is strongly absorbed by ozone.

The ratio of photon counts in the rotational Raman channels is given by

$$\frac{S_{RR}(\lambda_1, J)}{S_{RR}(\lambda_2, J)} = \frac{d\sigma_J/d\Omega(\lambda_1)}{d\sigma_J/d\Omega(\lambda_2)} \left(\frac{\tau(\lambda_1)}{\tau(\lambda_2)} \right)^2 \frac{K(\lambda_1)}{K(\lambda_2)} \frac{S_0(\lambda_1)}{S_0(\lambda_2)} \qquad (10.30)$$

where $S_{RR}(\lambda_i, J)$ are the numbers of photon counts detected and $S_0(\lambda_i)$ are the numbers of photons transmitted by the lidar. J is the rotational quantum number, $K(\lambda_i)$ denote the receiver efficiencies, $(d\sigma_J/d\Omega)(\lambda_i)$ are the differential cross sections for pure rotational Raman backscattering, and $\tau(\lambda_i)$ are the transmissions of the atmosphere with $i = 1, 2$ and the primary wavelengths $\lambda_1 = 532$ nm and $\lambda_2 = 355$ nm. (The atmospheric transmission is approximately constant within the pure rotational Raman spectrum of one primary wavelength.)

The ratio of rotational Raman cross sections is

$$\frac{d\sigma_J}{d\Omega}(\lambda_1) \Big/ \frac{d\sigma_J}{d\Omega}(\lambda_2) \approx (\lambda_2/\lambda_1)^4 = (2/3)^4 \approx 0.2. \qquad (10.31)$$

Ozone absorption is <2% for λ_1 and <0.5% for λ_2 up to 30 km height [63]. So differences in ozone absorption can be neglected and the most important term that depends on height z for this comparison is the atmospheric transmission due to Rayleigh extinction. It is described by

$$\tau_{\text{Ray}}(z) = \exp\left(-\int_{z_0}^{z} N(\zeta)\sigma_{\text{Ray}}(\lambda)d\zeta\right), \qquad (10.3)$$

where $N(\zeta)$ is the molecular number density at height ζ. It is taken here from a standard atmosphere. The total Rayleigh cross section can be calculated with

$$\sigma_{\text{Ray}}(\lambda) = \frac{8\pi^3(n(\lambda)^2 - 1)^2}{3\lambda^4 N_s^2}\left(\frac{6+3\gamma}{6-7\gamma}\right) \qquad (10.32)$$

where $\gamma = 0.0279$ is called "depolarization factor," $N_s = 2.547 \times 10^{25}$ m^{-3} is the molecular number density, and n is the refraction index of air (both at standard conditions) with $n(\lambda_1) - 1 = 2.78197 \times 10^{-4}$ and $n(\lambda_2) - 1 = 2.85706 \times 10^{-4}$ [64, 65].

Typical values of the transmissions of the optical components in the receivers and typical detector efficiencies yield a ratio

$$\frac{K(\lambda_1)}{K(\lambda_2)} \approx 2. \qquad (10.33)$$

For the same laser power, the ratio of the number of emitted photons is then given by

$$\frac{S_0(\lambda_1)}{S_0(\lambda_2)} = 1.5. \qquad (10.34)$$

If laser pulse energies are the same for the two wavelengths, we thus have

$$\frac{P_{\text{RotRam}}(\lambda_1, J)}{P_{\text{RotRam}}(\lambda_2, J)} = 0.6T^*(z) \qquad (10.35)$$

with the height-dependent term

$$T^*(z) = (\tau(\lambda_1)/\tau(\lambda_2))^2 \qquad (10.36)$$

which describes the effect of atmospheric transmission.

$T^*(z)$ and $S_{\text{RR}}(\lambda_1, J)/S_{\text{RR}}(\lambda_2, J)$ as a function of height are shown in Fig. 10.4. Rotational Raman signals from altitudes above 20 km are ~60% stronger if a primary wavelength of $\lambda_1 = 532$ nm instead of $\lambda_2 = 355$ nm is used. This means that it is advantageous to use 532 nm as the
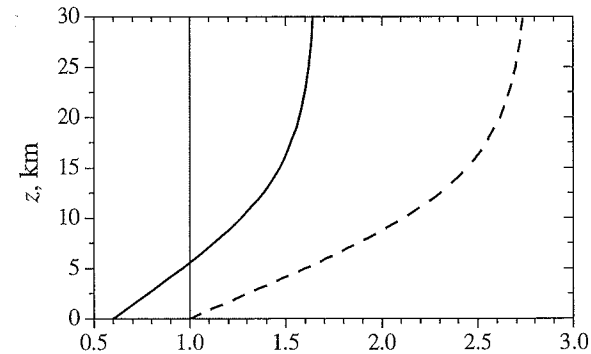
Fig. 10.4. Calculated ratio of rotational Raman signal intensities $S_{\text{RR}}(\lambda_1, J)/S_{\text{RR}}(\lambda_2, J)$ (solid curve) and atmospheric transmission factor $T^*(z)$ (dashed curve) versus height z with primary wavelengths $\lambda_1 = 532$ nm and $\lambda_2 = 355$ nm for equal laser power (see text for further details).

primary wavelength for a system aiming at high performance in the upper troposphere and in the stratosphere, whereas 355 nm is better suited for temperature measurements in the lower troposphere if the same laser power is available at both wavelengths. These results, however, were obtained under the assumption of Eq. (10.33). With future improvements in receiver technology, this assumption must certainly be reevaluated, which will extend the range for which UV primary wavelengths are superior for RR lidar. First measurements with a system not yet optimized were very promising and have already shown the general feasibility of using 355 nm as the primary wavelength for RR lidar [66].

In addition to signal intensity, it is also important to consider possible differences of the blocking of the elastic backscatter light in the RR channels. The molecular elastic backscatter signal is proportional to λ_0^{-4}, just like the pure rotational Raman signal. Thus no differences in relative signal intensity exist and the relative blocking required for merely the molecular elastic signal is independent of laser wavelength. For particle backscattering, the wavelength dependence varies with size, composition, and shape of the particles. One simplifying rule says that, if the average particle size is significantly larger than both laser wavelength (which is the case for most types of clouds and many types of aerosols), then the relative intensity of the particle signal is lower in the UV than in the visible. There is thus an advantage for a UV primary wavelength under the same atmospheric conditions. On the other hand, the blocking of the elastic backscatter signal in the RR channels that can be achieved today is also lower in the UV which tends to compensate that advantage.

Required Suppression of the Elastically Backscattered Light in the Rotational Raman Channels

The major technical challenge for temperature measurements with the rotational Raman technique is to achieve sufficient blocking of the elastic backscatter signal in the rotational Raman channels. The problem is particularly serious in the low-J channel because of its close proximity ($<30\,\text{cm}^{-1}$ or $<1\,\text{nm}$ at $\lambda = 532\,\text{nm}$). In this section we present a calculation which attenuation is needed. This point has risen considerable controversy in the literature [42, 67]. We show that to ensure measurement errors $<1\,\text{K}$ in clouds up to a backscatter ratio (R_{532}) of 50, a blocking by at least seven orders of magnitude is required. This requirement can be met in practice with today's state-of-the- art optics (see Section 10.5).

The backscatter ratio R_{532} is defined as the ratio of total backscatter intensity to molecular backscatter intensity.* The optical thickness χ of the rotational Raman channels at the primary wavelength λ_0 is

$$\chi = -\log_{10}(\tau(\lambda_0)) \tag{10.37}$$

where $\tau(\lambda_0)$ is the filter transmission. For the calculation, we first simulate the pure rotational Raman signal of air for different temperatures. Then we multiply the spectra with the transmission curves of the receiver channels to get the intensities of the unperturbed rotational Raman signals. The results are used for deriving the calibration function. We add an offset to the unperturbed signals of a single input temperature according to the assumed leakage of the elastic signal. The "measured" temperature is then calculated with the perturbed signals via the calibration function. The leakage measurement error is the difference between the input temperature and the temperature which would be measured with the signals including elastic-signal leakage.

As an example, Fig. 10.5 shows the results of such a calculation for a backscatter ratio $R_{532} = 50$ and input temperatures of 180 K and 250 K and the receiver parameters taken from Ref. 46. The leakage measurement error is zero if the ratio of elastic offset signals is the same

---

* The backscatter ratio, i.e., the ratio of total backscatter signal to molecular backscatter signal, is not consistently defined in the literature. Depending on the system in use, different receiver spectral widths result in the extraction of different fractions of the pure rotational Raman spectrum (PRRS) for the total backscatter signal. As the PRRS is about 3% of the total molecular backscatter signal the differences, however, are small.
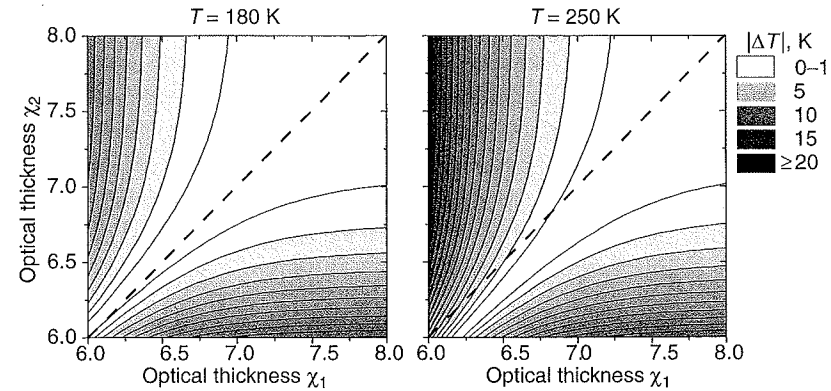
Fig. 10.5. Calculated leakage measurement error ΔT for $R_{532} = 50$ versus the primary-wavelength optical thicknesses χ_1 and χ_2 of the two rotational Raman channels for two "input" temperatures, $T = 180\,\text{K}$ and $T = 250\,\text{K}$. Error contour lines are plotted at intervals of 1 K. Absolute values are given. ΔT is negative in the upper left and positive in the lower right region of the plots. Dashed lines mark $\chi_1 = \chi_2$.

as the ratio of the unperturbed rotational Raman signals. This illustrates directly that the leakage error itself depends on temperature and on the parameters of the individual receiver. If the RR signal intensities are approximately the same within the range of atmospheric temperatures, similar values of elastic backscatter signal blocking are desirable. Ironically, a combination of a lower blocking in one and a higher blocking in the other channel may result in a larger leakage error than the same lower blocking value in both channels.

Figure 10.6 shows leakage errors for equal blocking χ of the two RR channels for different values of "input" temperature. Even if the
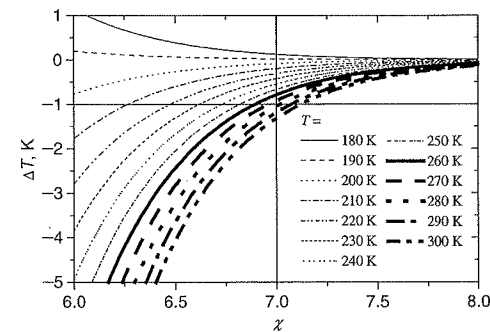

Fig. 10.6. Calculated leakage measurement error ΔT for $R_{532} = 50$ against optical thickness of the two rotational Raman channels $\chi = \chi_1 = \chi_2$ at different temperatures T.

blocking for both RR channels is the same, the sign of the leakage errors is not necessarily the same for all temperatures. With the filter parameters used for this calculation, which may be considered as typical for RR lidar, $|\Delta T|$ is <1 K between 180 and 280 K for $R_{532} = 50$ with $\chi \geq 7$ for both rotational Raman channels. In conclusion, if the elastic backscatter signal is blocked in the RR channels by at least seven orders of magnitude, leakage errors are small even in heights of significantly enhanced particle backscatter signals.

Center Wavelengths and Bandwidths of the RR Channels

Next, we investigate the important question which filter center wavelengths (CWL_{RR1} and CWL_{RR2}) and channel passbands (full-width-at-half-maximum bandwidths $FWHM_{RR1}$ and $FWHM_{RR2}$) yield the minimum statistical temperature error of RR temperature measurements. We can limit the calculations to combinations of the filter parameters with CWL_{RR1}, CWL_{RR2} in regions of opposite temperature dependence and $FWHM_{RR1}$, $FWHM_{RR2}$ sufficiently small that λ_0 is out of the filter transmission band.

The majority of today's RR lidar systems extract parts of only the anti-Stokes branch of the pure rotational Raman spectrum (PRRS) in order to avoid the risk of interference with aerosol fluorescence. In addition, when anti-Stokes signals are extracted and an interference-filter-based receiver is employed, the distance of the filter center wavelengths to the laser wavelength can be increased by increasing the angle of incidence onto the filters. This allows to fine-tune the transmission wavelength when the blocking at the laser wavelength must be increased.

The 1-σ uncertainty of a photon counting signal S follows Poisson statistics and is therefore given by

$$\Delta S = \sqrt{S}, \qquad (10.38)$$

which yields, for the uncertainty of the RR temperature measurement,

$$\Delta T = \frac{\partial T}{\partial Q} Q \cdot \sqrt{\frac{1}{S_{RR1}} + \frac{1}{S_{RR2}}}$$

$$= \left(\frac{\partial S_{RR1}}{\partial T} \frac{1}{S_{RR1}} - \frac{\partial S_{RR2}}{\partial T} \frac{1}{S_{RR2}} \right)^{-1} \sqrt{\frac{1}{S_{RR1}} + \frac{1}{S_{RR2}}}, \qquad (10.39)$$

where

$$Q = \frac{S_{RR2}}{S_{RR1}} \qquad (10.24)$$

is the ratio of the two signals S_{RR1} and S_{RR2} of lower and higher RR quantum-number transition channels. We can approximate the derivatives in Eq. (10.39) with the corresponding differences such that

$$\frac{\partial T}{\partial Q} \approx \frac{T_2 - T_1}{Q(T_2) - Q(T_1)}. \qquad (10.40)$$

It is appropriate to use a peak transmission $\tau = 1$ and an out-of-band transmission $\tau = 0$ in this simulation. With the use of, e.g., Gaussian-shaped filter transmission curves to account for the slope of the filter edges, the resulting data would just be smoother, which would neither improve the clarity of the results nor change the conclusions.

Figure 10.7 shows the temperature sensitivity

$$\frac{\partial S}{\partial T} \approx \frac{S(T_2) - S(T_1)}{T_2 - T_1}, \qquad (10.41)$$

for different parts of the RR spectrum when $T_1 = 235$ K and $T_2 = 240$ K. For these temperatures, regions with negative sign of $\partial S/\partial T$ are found at center wavelengths between ~530.5 nm and ~534.5 nm and positive
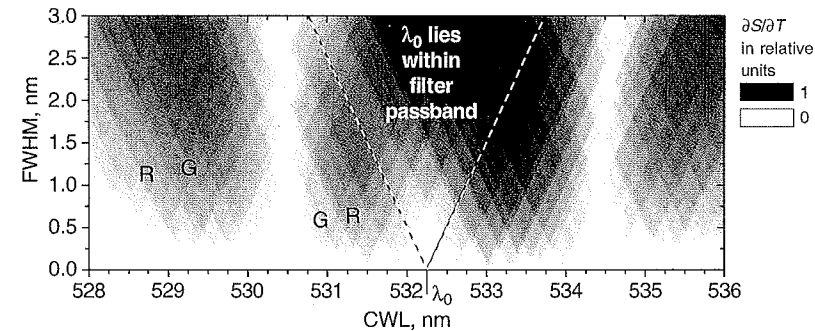

Fig. 10.7. Calculated temperature sensitivity $\partial S/\partial T$ of atmospheric pure rotational Raman signals versus center wavelength CWL and bandpass full width at half maximum FWHM. The laser wavelength λ_0 was set to 532.25 nm, temperatures to $T_1 = 235$ K and $T_2 = 240$ K. Calculation stepwidth was 0.025 nm. Absolute values only are plotted; $\partial S/\partial T$ is negative for CWLs between ~530.5 nm and ~534.5 nm and positive elsewhere. The parameters of two interference-filter-based RR lidars are marked with 'G' [46] and 'R' [48], respectively.